Pengbo Su
State Key Laboratory for Strength and Vibration of Mechanical Structures, Xi'an Jiaotong University, Xi'an, Shaaanxi 710049, China; School of Mechanical Engineering, Xi'an Jiaotong University, Xi'an, Shaaanxi 710049, China; State Key Laboratory of Mechanics and Control of Mechanical Structures, Nanjing University of Aeronautics and Astronautics, Nanjing 210016, China
e-mail: su_pengbo@126.com

Bin Han[1]
School of Mechanical Engineering, Xi'an Jiaotong University, Xi'an, Shaaanxi 710049, China; Research Institute of Xi'an Jiaotong University, Zhejiang, Hangzhou 311215, China
e-mail: hanbinghost@xjtu.edu.cn

Mao Yang
State Key Laboratory for Strength and Vibration of Mechanical Structures, Xi'an Jiaotong University, Xi'an, Shaaanxi 710049, China
e-mail: 15050822354@163.com

Zhongnan Zhao
State Key Laboratory for Strength and Vibration of Mechanical Structures, Xi'an Jiaotong University, Xi'an, Shaaanxi 710049, China
e-mail: workzhaoqiansunli@163.com

Feihao Li
State Key Laboratory for Strength and Vibration of Mechanical Structures, Xi'an Jiaotong University, Xi'an, Shaaanxi 710049, China
e-mail: 925257128@qq.com

Qi Zhang
School of Mechanical Engineering, Xi'an Jiaotong University, Xi'an, Shaaanxi 710049, China
e-mail: henryzhang@xjtu.edu.cn

Qiancheng Zhang
State Key Laboratory for Strength and Vibration of Mechanical Structures, Xi'an Jiaotong University, Xi'an, Shaaanxi 710049, China
e-mail: zqc111999@mail.xjtu.edu.cn

Tian Jian Lu[1]
State Key Laboratory of Mechanics and Control of Mechanical Structures, Nanjing University of Aeronautics and Astronautics, Nanjing 210016, China;

Energy Absorption of All-Metallic Corrugated Sandwich Cylindrical Shells Subjected to Axial Compression

The energy adsorption properties of all-metallic corrugated sandwich cylindrical shells (CSCSs) subjected to axial compression loading were investigated by the method combining experiments, finite element (FE) simulations, and theoretical analysis. CSCS specimens manufactured using two different methods, i.e., high-speed wire-cut electric discharge machining (HSWEDM) and extrusion, were tested under axial compression. While specimens fabricated separately by HSWEDM and extrusion both exhibited a stable crushing behavior, the extruded ones were much more applicable as lightweight energy absorbers because of their good energy absorption capacity, repeatability, and low cost. The numerically simulated force–displacement curve and the corresponding deformation morphologies of the CSCS compared well with those obtained from experiments. The specific folding deformation mode was revealed from both experiments and simulations. Subsequently, based upon the mode of folding deformation, a theoretical model was established to predict the mean crushing force of the CSCS construction. It was demonstrated that CSCSs with more corrugated units, smaller value of t_c/t_f and W/R_o could dissipate more impact energy. Such sandwich cylindrical shells exhibited better energy absorption than monolithic cylindrical shells, with an increase of at least 30%. Ultimately, the dynamic effect under the impact load was further evaluated. The dynamic amplification coefficient of CSCS decreased with the increase of the wall thickness. [DOI: 10.1115/1.4048200]

Keywords: sandwich cylindrical shells, different fabrication methods, energy absorption, theoretical model, dynamic effects

[1]Corresponding authors.

Contributed by the Applied Mechanics Division of ASME for publication in the JOURNAL OF APPLIED MECHANICS. Manuscript received June 22, 2020; final manuscript received August 12, 2020; published online September 17, 2020. Assoc. Editor: Hareesh Tippur.

Nanjing Center for Multifunctional
Lightweight Materials and Structures (MLMS),
Nanjing University of Aeronautics and
Astronautics,
Nanjing 210016, China
e-mail: tjlu@nuaa.edu.cn

1 Introduction

Along with continuously increasing operation speed of transportation vehicles, especially in bullet trains, collision safety becomes a critical issue. Thin-walled metallic structures have been extensively used to construct energy absorbing systems due to high weight ratio, low cost, and attractive energy absorption [1]. During collision, these structures can absorb significant amounts of kinetic energy via plastic deformation to improve passenger survivability. Existing research on the energy absorption of thin wall structures mainly focus on single-cell, multi-cell, and foam-filled tubular structures [2].

Single-cell tubular structures, which collapse in progressive folding when subjected to axial impact, had been studied extensively [3–8]. Alexander [3] first presented a theoretical model to determine the mean crushing force of a cylindrical shell collapsing in the concertina mode. By introducing the curvature of folding length to Alexander's solution, an improved theoretical model was subsequently developed, which included the effective crushing length [4,5]. For rectangular tubes, a basic folding mode was proposed for the in-extensional collapse mode named as "super folding elements," consisting of toroidal surface, horizontal hinge line, and inclined traveling hinge line [6]. With plastic energy dissipated in the folding elements, the mean crushing force was calculated via energy balance. This approach was extended to cover extensional collapse modes [5,7] and arbitrary angled multi-corner prismatic columns [8]. Further, a variety of cross-sectional shapes have been extensively studied for single-cell tubular structures, such as the polygonal shape [9–13], the star shape [14], the sinusoidal shape [15], and the non-convex multi-corner shape [16].

For rectangular tubes, it was observed that a large quantity of kinetic energy was dissipated in the toroidal surface and the inclined traveling hinge line, which were formed near the corner zones [6]. Thus, the number of corners on tubular section greatly affects the energy absorption performance of a tubular structure [6]. Besides, the presence of corners enclosed in the tubular structure is beneficial for stable progressive folding deformation [17]. Therefore, extensive studies about the crushing behaviors of multi-cell tubular structures had been carried out. For typical instance, the crushing responses of single-cell, double-cell, and triple-cell tubular structures under axial compression were investigated and compared [18], with closed-form solution of mean crushing force presented for each type of tubular structure; based on the method of "super folding elements," a simplified folding mode to calculate the mean crushing force was proposed for square multi-cell tubular structures [19]. Further research on the crushing resistance of angle elements were also carried out [20–22]. For additional improvement in energy absorption efficiency, novel designs were also proposed, e.g., multi-cell tubes with lateral variable thickness [23], multi-corner tubes with bulkheads [24], and hierarchical lattice topology tubes [25].

Meanwhile, it has been demonstrated that tubular structures filled with cellular materials, such as foams and honeycombs, led to enhanced energy absorption in comparison with those without fillers. The low density and constant stress when compressed make high porosity cellular materials ideal filling materials for thin-walled tubular structures. Interaction effects between filling materials and tubular walls were found to be the main mechanism underlying significant increase in energy absorption [19]. Tubular structures filled with conventional polyurethane foams [26–28], aluminum foams [29–32], and honeycombs [31,33] were studied. More recently, functionally graded materials were introduced as the filling material to improve the crushing stability of energy absorption structures [34–37].

However, a great amount of thin-walled tubular materials mentioned above do not undergo much large plastic deformation [38]. In addition to these tubular structures, sandwich panels cored with cellular materials, such as periodic lattice trusses and hybrid lattice trusses, had been extensively investigated for their high energy absorption capacity and weight saving in the field of impact protection [39–46]. To further improve the energy absorption performance, cellular material filled bi-tubal structures were also envisioned, which may be named as sandwich shells. The energy absorption properties of sandwich polygonal shells having foam-filled cores were studied numerically and it was found that these structures exhibit outstanding energy absorption characteristics [47]. Zhang et al. [2,38] investigated the crushing behavior of honeycomb filled sandwich cylindrical shells and found that these structures were excellent energy absorbers. Thus far, numerical simulation with the method of finite elements (FEs) has been the main method used in previous studies, except for the study of Liu et al. [48], who fabricated all-metallic sandwich shells with star-shaped tube cores and experimentally characterized their energy absorption properties. However, in their study, the cores and the facesheets were not bonded, causing insignificant coupling effects between the two. Other researchers fabricated sandwich cylindrical shells having fiber-reinforced composite lattice cores and investigated the strength and vibration responses of such structures [49–54], but did not explore their energy absorption characteristics.

In our previous study [55], thin-walled corrugated sandwich cylindrical shells (CSCSs) made of 1060 aluminum were manufactured by the method involving tamping and shape correction, in which the thickness of facesheets/cores was 0.4 mm/0.2 mm or 0.2 mm/0.1 mm; all the components were then bonded using structural adhesive. Consequently, at large deformation, debonding of the adhesive interface could not be avoided, which weakened the coupling effects between facesheets and corrugated core webs and thus energy absorption. In addition, there was yet a theoretical analysis to explore the energy absorbing mechanisms of the CSCSs. It should also be mentioned that, with the previous preparation method, the upper limit of wall thickness was ~0.4 mm due to the inevitable springback during fabrication. To address these deficiencies, further developments were conducted in the present study. New CSCS specimens were manufactured using two completely different methods, i.e., high-speed wire-electrode discharge machining and extrusion process, so that debonding between facesheets and core members were avoided and the wall thickness could exceed 1 mm. More stable crushing behaviors of the CSCSs were therefore expected particularly at large deformations, in comparison with the thin-walled ones in our former work [55]. To predict the mean crushing force of the structure, the folding deformation mode was explored in detail and a theoretical model was developed. In addition, the effects of impact velocity and wall thickness on energy absorption were discussed.

2 Terminology of Axial Crushing

When subjected to axial compression, the typical crushing behavior of a thin-walled monolithic cylindrical shell and the corresponding terminology are depicted in Fig. 1. Let H_s represent the original height of the shell and d denote the actual crushing distance. The absorbed energy at d is defined as $E(d)$. Let the mean crushing force and maximum force in the interval (0–d) be named as $F_m(d)$ and $F_{max}(d)$, respectively. The total energy absorption efficiency $T_E(d)$ is defined as the quotient of $E(d)$ and $F_{max}(d)$ [29]. The maximum efficiency is reached when $T_E(d)$ is maximized. Let the crushing distance corresponding to the maximum $T_E(d)$ be defined as d_{max}. Correspondingly, F_m and F_{max} at d_{max} refer to the mean crushing force and the maximum force in the entire crushing behavior, as expressed in Eq. (1). In addition, the crushing force efficiency A_E and the stroke efficiency S_E are defined in Eq. (2)

$$F_m = F_m(d_{max})\ F_{max} = F_{max}(d_{max}) \tag{1}$$

$$A_E = \frac{F_m}{F_{max}}\ \ S_E = \frac{d_{max}}{H_s} \tag{2}$$

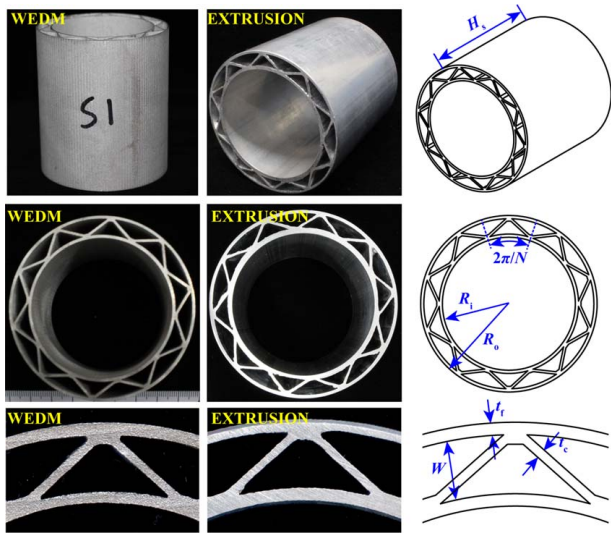

Fig. 2 Corrugated core sandwich cylindrical shells fabricated by HSWEDM and the extrusion process

3 Experiments

3.1 Specimen Preparation and Experimental Procedure. Corrugated core sandwich cylindrical shells were fabricated by either high-speed wire-electrode discharge machining (HSWEDM) or extrusion process (Guangdong Jiahua Aluminum Profile Co., Ltd.), as shown in Fig. 2, with shell height H_s = 80 mm, radius of outer facesheet R_o = 35 mm, radius of inner facesheet R_i = 27.5 mm, core width W = 5 mm, facesheet thickness t_f = 1.2 mm, and core web thickness t_c = 1.0 mm. HSWEDM and extrusion are both mature fabrication processes for metal materials. For HSWEDM, the threading holes for cutting wire in the 6061 aluminum bar were fabricated by the drilling machine in the first place. Then, according to the designed cross section, unwanted material was removed from the aluminum bar by the rapidly recurring cutting wire, which was placed between the two electrodes. The process of extrusion began by heating the 6063 aluminum bar to 450 °C. Then the heated bar was transferred into the 1500 tons extrusion equipment. A ram applied the pressure to the dummy block, in turn, pressed the aluminum bar to push it through the die of the designed cross section with the extrusion speed of 1.5m/min. Finally, the extruded bar was cut into CSCS samples after the precipitation heat treatment (205 °C, 1 h). It can be seen in Fig. 2 that the sandwich shells prepared by these two processes were integrally formed, in which the corrugated core and the facesheets were directly connected by the base material, rather than adhesive bonding or welding. The strength and toughness of the aluminum itself were much better than the adhesive layer or the welding layer. Thus, the debonding phenomenon in our previous study [55] could be avoided to the utmost.

Given the formability of parent material, aluminum 6061T4 and 6063T5 were separately used for high-speed wire-electrode discharge machining (HSWEDM) and extrusion. The tensile tests of each material were carried out following ASTM Standard E8M-04 and the corresponding material properties were presented in Fig. 3. The power strengthening model of 6063T5 was also given in Fig. 3 to calculate the flow stress, which was used in subsequent theoretical analysis.

Quasi-static axial compression tests of as-fabricated CSCS specimens were carried out using the setup of Fig. 4. The upper pressure plate was fixed, while the lower pressure plate was moved upward to compress the test specimen at a rate of 1 mm/min. The exerted crushing distance and the reaction force in the pressure plate were acquired with a data acquisition system. Besides, a video capture system companied with a lighting equipment was used to access the deformation evolution of each specimen under axial compression. Three identical specimens from each fabrication method

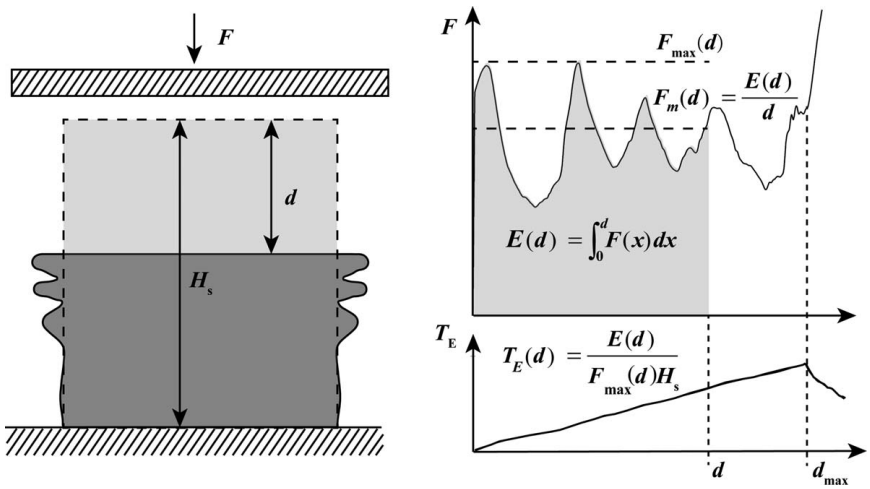

Fig. 1 Terminology in a typical crushing behavior of thin-walled monolithic cylindrical shell

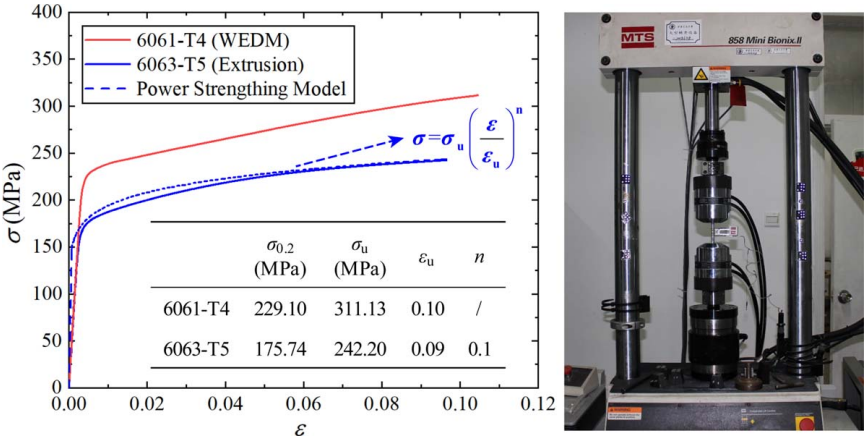

Fig. 3 Material properties obtained for 6061T4 and 6063T5 from quasi-static uniaxial tension

were tested. The HSWEDM specimens were denoted as W1–W3, while the extrusion specimens as E1–E3.

3.2 Experimental Results. Figure 5 presented the experimentally measured force versus displacement curves of W1–W3 and E1–E3, together with representative deformation configurations indicating the deformation history. Final configurations of the specimens were displayed in Fig. 6, whereas high magnification views of their surfaces were presented in Fig. 7. Corresponding values of F_m, F_{max}, A_E, and S_E are listed in Table 1.

As shown in Fig. 5, the force versus displacement curves for both groups of CSCS specimens exhibited good repeatability. Thus, for brevity, only representative deformation configurations at different compressive strains were displayed for each group. It could be seen from Figs. 5(*c*) and 5(*d*) that all specimens showed five folds along the axial direction and the deformation behavior during compression were almost the same. Under compression, the force versus displacement curve initially underwent a linear stage before reaching the peak force. After the peak force was reached, a sudden drop followed until point I where the first fold was formed. With further compression, additional folds (four in total; Fig. 5) formed in a similar deformation process, with alternating peak and valley loads appearing in the curve. The final configurations of all the specimens after compression as shown in Fig. 6 were also similar, except for the ruptures observed in HSWEDM specimens. It was noticed that an axisymmetric folding mode formed and the folds expanded to ten sub-folds along the circumferential direction of each specimen. This folding mode was referred to here as the "localized axisymmetric folding mode," which was also identified in our previous work [44].

Although the deformation processes and final deformation configurations of the two specimens groups were similar, there were some differences induced by the different fabrication methods as well as different material makes. It was indicated from Figs. 6(*d*)–6(*f*) that the extrusion specimens had good ductility without ruptures. Moreover, the final configurations, load versus displacement curves and corresponding calculated parameters were highly consistent for each extrusion specimen. On the contrary, local ruptures were observed in all the specimens fabricated via HSWEDM (Figs. 6(*a*)–6(*c*)), especially in W3. As shown in Fig. 6(*c*), the fracture failure of W3, also named as a "zipper type" failure, was induced which started from either the top or bottom of specimen W3 and gradually developed along its axial direction like opening a zipper [30]. Ruptures occurred during crushing had direct effects on the force versus displacement curves of the HSWEDM specimens. It could be seen from Figs. 5(*a*) and 5(*b*) that curves of the HSWEDM specimens did not exhibit the same good consistency as the extrusion ones. However, as shown in Table 1, the mean crushing forces of the HSWEDM specimens were not influenced obviously by these ruptures, for most of the regions in these specimens enjoyed relatively stable deformation. It could also be seen from Table 1 that the extrusion specimens had a higher value of A_E, indicating better energy absorption.

To further explain the differences arising from the preparation process, Fig. 7 displayed high magnification cross-sectional views of both HSWEDM and extrusion specimens. From Fig. 7(*b*), it was seen that the edges of the HSWEDM specimen were uneven,

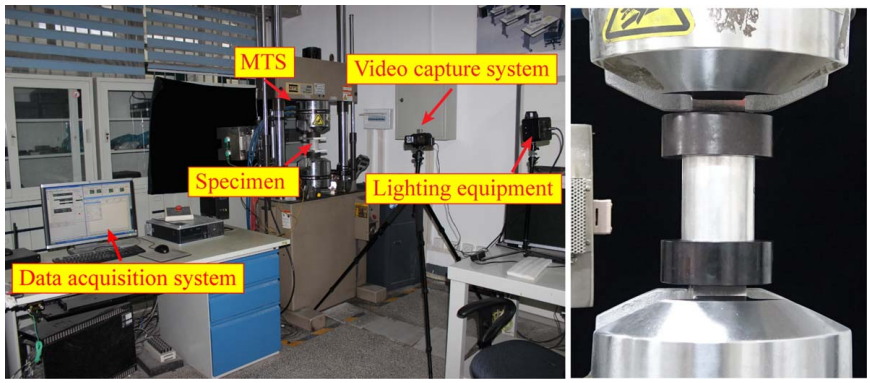

Fig. 4 Experiment setup of CSCS specimen subjected to quasi-static axial compression

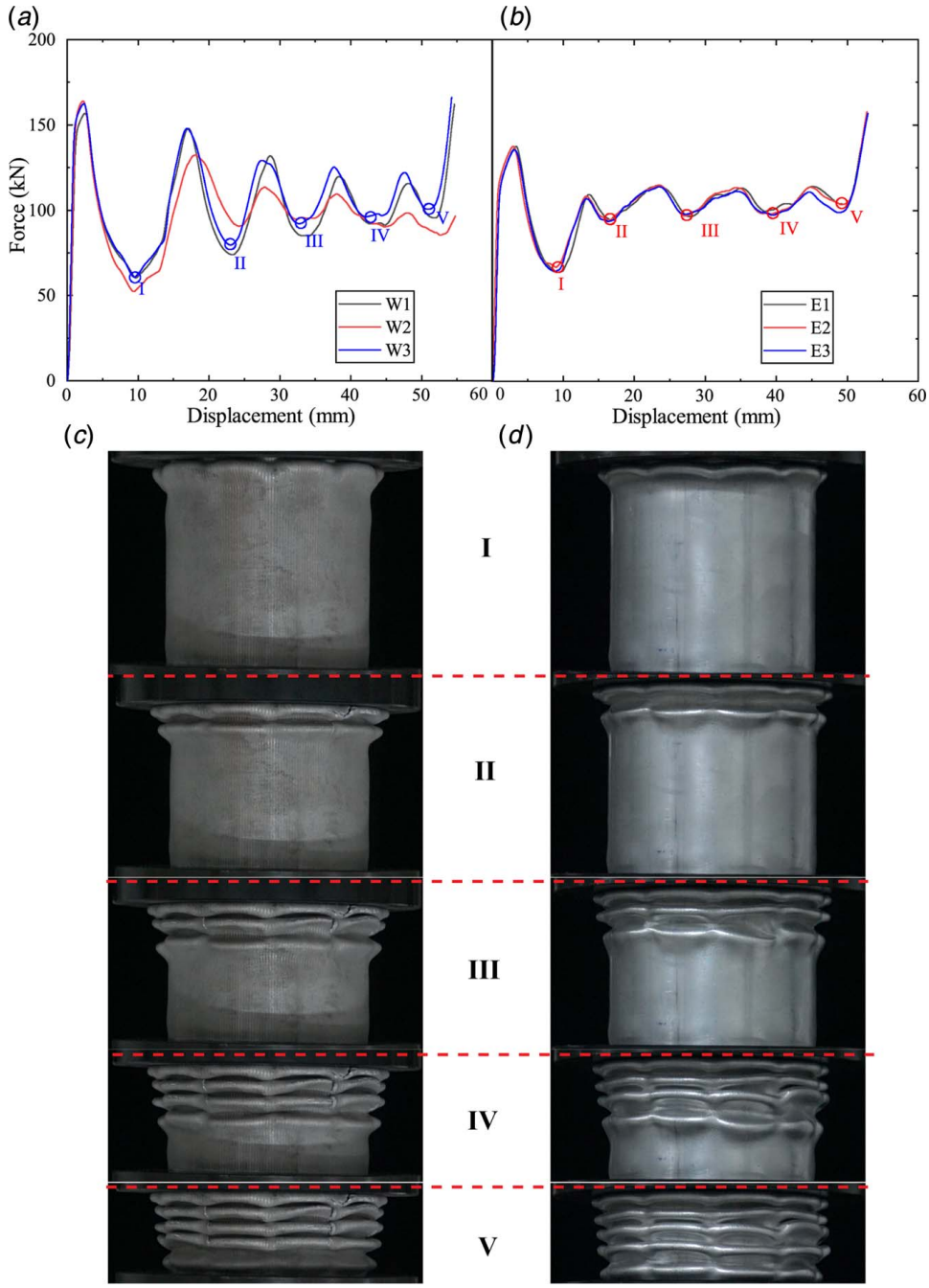

Fig. 5 Force versus displacement curves of (*a*) W1–W3 and (*b*) E1–E3 specimens; representative deformation configurations of (*c*) W1 and (*d*) E1 specimens

looking like serrations. These serrations at the edges were prone to cause crack initiation and propagation during compression, with local ruptures gradually developed along the crack at sufficiently large compressive strains. The uneven edges might be induced by non-even wire tension during the HSWEDM. On the contrary, the extrusion specimen exhibited even and smooth edges. Therefore, the extrusion specimens enjoyed better ductility than those made via HSWEDM.

Overall, the better energy absorption capacity and repeatability made the extrusion CSCSs a more ideal energy absorption structure compared with the HSWEDM ones. Besides, the fabrication costs of the former were relatively low, because the unit price of extrusion parts was about one tenth of that of HSWEDM parts when the quantity of the production exceeded 1000. Additional comparison of the two different fabrication methods was presented in the Appendix.

4 Numerical Simulations

In this section, FE simulations were conducted to explore the mechanisms underlying folding deformation, which was somewhat periodic (Figs. 5 and 6), as observed during compressive tests. Only extrusion specimens were considered, as they exhibited better experimental repeatability.

4.1 The Finite Element Model. Numerical simulations corresponding to the present experiments were conducted with ABAQUS/EXPLICIT. In the FE model shown in Fig. 8(*a*), the pressure plates were modeled as rigid plates. Eight-node solid elements (C3D8R) were used for both the facesheets and the corrugated core, with element size 0.3 mm × 0.3 mm × 0.3 mm. A mesh sensitivity study was carried out to identify the minimal element size needed

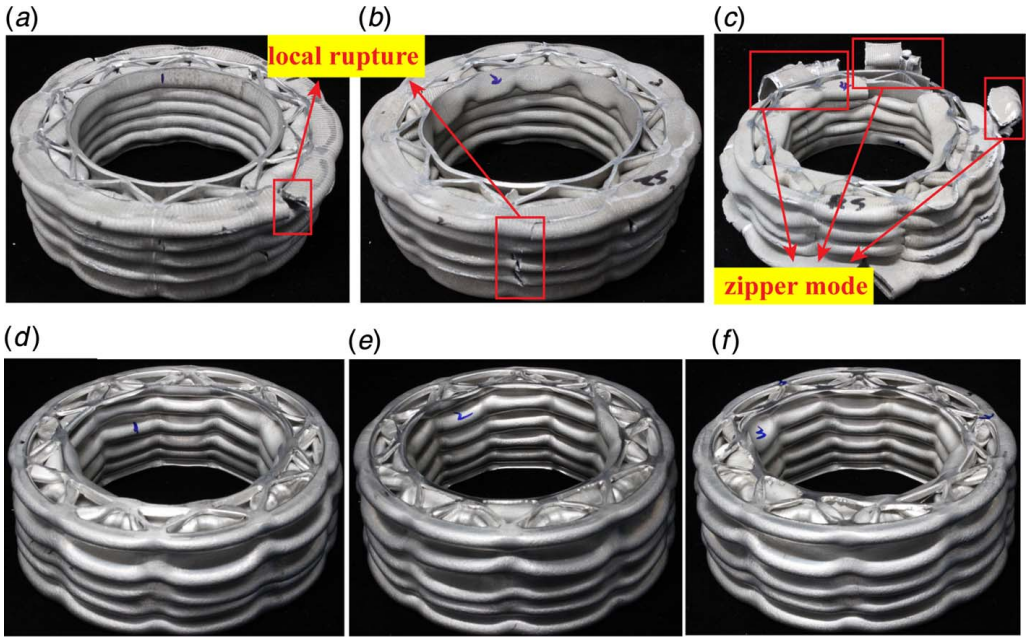

Fig. 6 Photos of CSCS specimens after compression: (*a*) W1, (*b*) W2, (c) W3, (*d*) E1, (*e*) E2, and (*f*) E3

for numerical convergence, which was shown in Fig. 8(*b*). In the finite element model, general contact was used between all the contacting surfaces with the Coulomb friction coefficient fixed at 0.2. The bot pressure plate was assumed to be fixed and the top pressure plate was moved along the 1-direction (i.e., axial direction; Fig. 8), at a sufficiently slow speed of 1 m/s. It has been valid (results not shown for brevity) that the kinetic energy in the whole model was quite small compared with the plastic dissipation during the crushing process, suggesting that the loading process in the simulation could be treated as the quasi-static crushing process. The 6063T5 aluminum was modeled as an isotropic solid and obeyed the von Mises J_2-flow theory, with relevant material parameters obtained from Fig. 3.

4.2 Validation Against Experiment Results. Figure 9 compared the numerically simulated force versus displacement curve and deformation configuration with those obtained from experiments. The simulated curve showed a qualitative agreement with the experimental curve; Fig. 9(*a*). The peak and valley trends of the two curves coincided quite well. Based on the curve, the numerically calculated values of F_m, F_{max}, A_E, and S_E were displayed in Table 1. It was seen that the difference between experimental and simulated results were small and acceptable. As presented in Fig. 9(*b*), the simulated final collapse configuration was almost identical as that observed in the experiment: there were in total five folds along the axial direction and ten sub-folds along the circumference for the CSCS specimen considered.

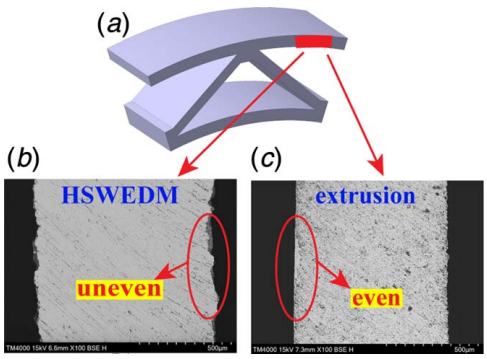

Fig. 7 High magnification cross-sectional view: (*a*) location on specimen, (*b*) HSWEDM specimen, and (c) extrusion specimen

4.3 The Folding Deformation. The present experimental and simulated results both indicated that axisymmetric collapse formed under axial compression. Here, two adjacent cells along the circumferential direction of the sandwich shell were used to explore the deformation mechanism underlying the formation of the first fold. As shown in Fig. 10, the blue lines represented the base configurations of undeformed cells (named as the base lines), while the red lines represented the folding lines of deformed cells in the first fold. With increasing compression, the folding lines gradually deviated from the base lines, indicating the actual folding deformation of both the facesheets and corrugated members. It should be noticed that all the red lines deviated from the blue lines to the same side, and this regularity was unique in CSCS structures. In Sec. 5, this novel folding mode was used to develop a theoretical model to predict the mean crushing force of CSCS structures.

5 The Theoretical Model

5.1 Basic Collapse Elements. Figures 11(*a*) and 11(*b*) presented the two basic collapse elements for folding deformation, i.e., the "super folding elements" for either in-extensional or extensional folding mechanisms. However, continuous and smooth displacement field for in-extensional mode is presented in Fig. 11(*c*) and the plastic flow of a metal sheet through a toroidal surface is

Table 1 Experimental and simulated results for all the CSCS specimens

	F_m (kN)	F_{max} (kN)	A_E	S_E
W1	100.22	156.93	0.63	0.68
W2	96.61	163.83	0.58	0.68
W3	104.97	161.96	0.64	0.68
E1	102.02	137.23	0.74	0.65
E2	102.35	137.57	0.74	0.65
E3	100.19	135.08	0.74	0.68
FE (extrusion)	115.5	150.76	0.76	0.67
Difference	13.7%	10.3%	2.7%	1.5%

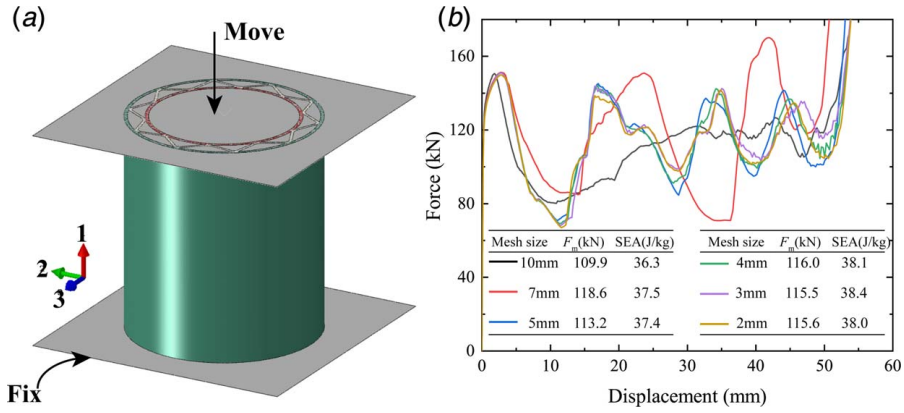

Fig. 8 (*a*) Finite element model of a CSCS specimen under axial compression and (*b*) results of convergence analysis

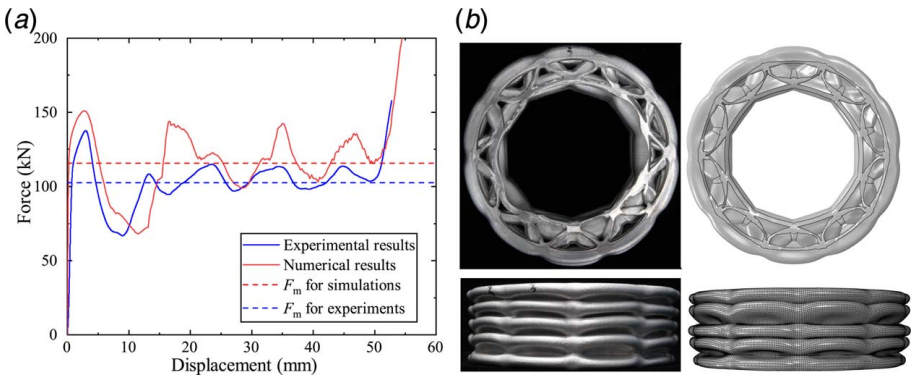

Fig. 9 Comparison between experimental and simulated results: (*a*) force versus displacement curves and (*b*) final deformation configurations (left for experiment and right for FE simulation)

shown in Fig. 11(*d*) [5,7,8]. The energy absorbed in the in-extensional basic folding element [8] was given by

$$E_1 = M_o(16HI_1b/h + 2\pi C + 4I_3H^2/b) \tag{3}$$

where

$$I_1 = \int_0^{\pi/2} \frac{d\phi}{\sqrt{\tan^2\psi_o + \cos^2\phi}} - \left(\frac{\pi}{2} - \psi_o\right) \tag{4}$$

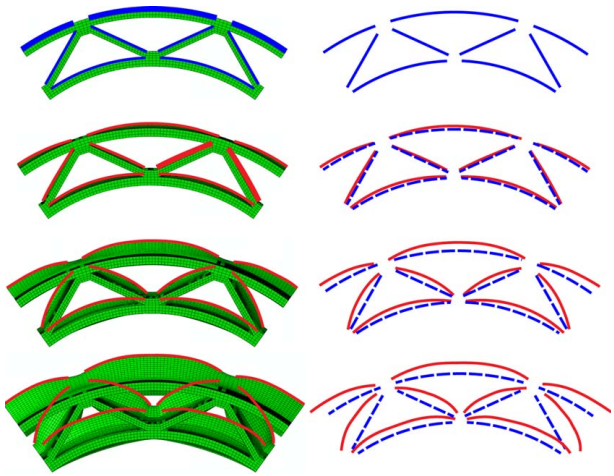

Fig. 10 Folding mode during formation of the first fold (Color version online.)

$$I_3 = \cot\psi_o \int_0^{\pi/2} \cos\alpha \sqrt{\tan^2\psi_o + \sin^2\alpha}\, d\alpha \tag{5}$$

Similarly, energy dissipation in the extensional collapse element [5,8] could be expressed as

$$E_2 = M_o\left[8\frac{H^2}{h}\left(\frac{\pi}{2} - \psi_o\right) + 2\pi C + 2H(\pi - 2\psi_o)\right] \tag{6}$$

5.2 Mean Crushing Force for Corrugated Sandwich Cylindrical Shells. As shown in Fig. 12(*a*), the curved cylindrical facesheets and corrugated panels in the cross section were simplified as a group of straight lines to calculate the dissipated energy [56]. Based on this simplification, folding deformation of the sandwich structure could be divided into four types of basic constituent element, named as I–IV in Fig. 12(*b*). The total absorbed energy of the entire sandwich structure was calculated by summing up the energy dissipation of each element. Each type of basic constituent element consisted of two plates, named as Panel A and Panel B in Fig. 12(*b*). As for type I–II, Panel A and Panel B referred to the facesheets and the corrugated core, respectively, while for type III–IV, both Panel A and Panel B referred to the facesheets.

Based on the folding deformation revealed from FE simulations (Fig. 10), the folding lines in the four constituent elements were determined, as illustrated in Fig. 12(*b*) with blue dash lines. According to the simulated folding mode displayed in Fig. 10, type I–II elements deformed in in-extensional folding mode (Fig. 11(*a*)), while type III–IV elements deformed in extensional folding mode (Fig. 11(*b*)). For a CSCS structure after compression, there were

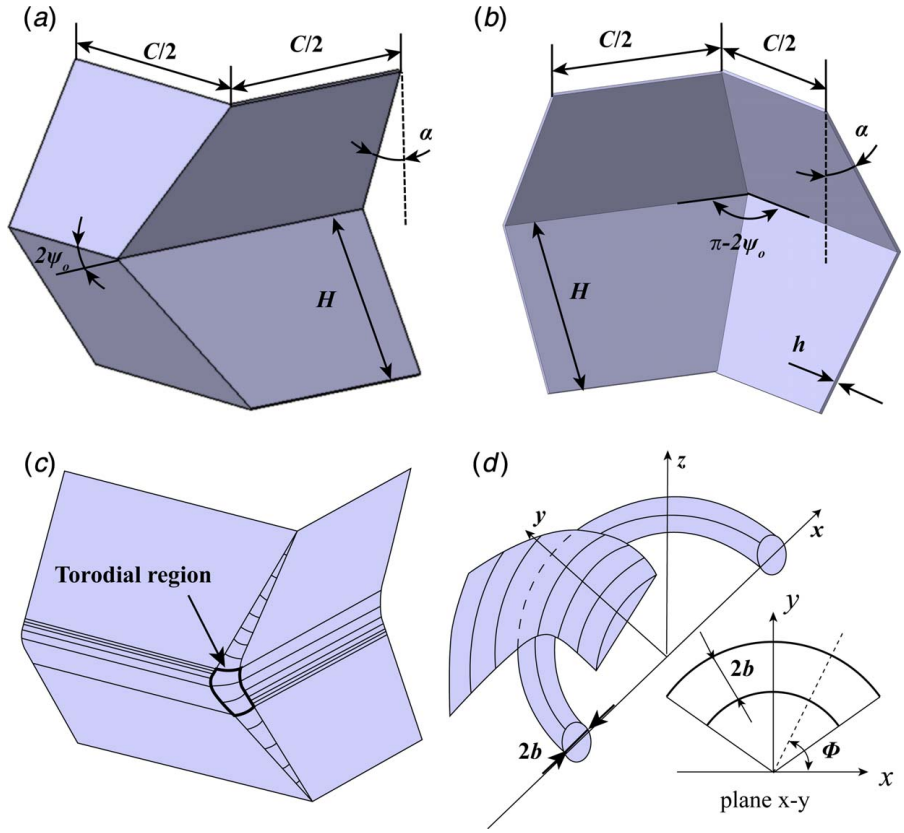

Fig. 11 (*a*) Basic collapse elements for in-extensional folding mechanisms, (*b*) basic collapse elements for extensional folding mechanisms, (*c*) basic collapse elements for in-extensional mode with continuous and smooth field, and (*d*) plastic flow of a metal sheet through a toroidal surface [5,7,8]

totally 20 type I–II constituent elements and 10 type III and type IV constituent elements, respectively. Energy dissipation of each constituent element could be calculated separately, based on the deformation mechanism of "super folding element," so as to determine theoretically the mean crushing force of the CSCS.

For type I elements deformed in in-extensional folding mode, the energy dissipated E_{I} could be written according to Eq. (3), as

$$E_{\mathrm{I}} = 1/16\sigma_{\mathrm{o}}(h_{\mathrm{IA}} + h_{\mathrm{IB}})^2(32HI_{\mathrm{I1}}b/(h_{\mathrm{IA}} + h_{\mathrm{IB}}) + 4I_{\mathrm{I3}}H^2/b) + 1/2\pi\sigma_{\mathrm{o}}(C_{\mathrm{IA}}h_{\mathrm{IA}}^2 + C_{\mathrm{IB}}h_{\mathrm{IB}}^2) \tag{7}$$

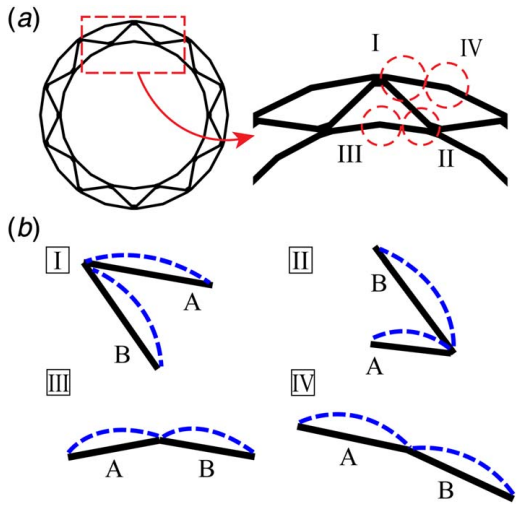

Fig. 12 Classification of folding elements

where

$$I_{\mathrm{I1}} = \int_0^{\pi/2} \frac{\mathrm{d}\phi}{\sqrt{\tan^2\psi_{\mathrm{Io}} + \cos^2\phi}} - \left(\frac{\pi}{2} - \psi_{\mathrm{Io}}\right) \tag{8}$$

$$I_{\mathrm{I3}} = \cot\psi_{\mathrm{Io}} \int_0^{\pi/2} \cos\alpha\sqrt{\tan^2\psi_{\mathrm{Io}} + \sin^2\alpha}\,\mathrm{d}\alpha \tag{9}$$

The subscripts I–IIII were added to the above equations in order to discriminate different types of element, while subscripts A and B represented different plates in one element. For example, h_{IA} indicated the thickness of plate A in type I element.

As the folding deformations for type I and type II elements were almost the same, the expression of energy absorption E_{II} was identical to type I and hence not displayed for brevity.

For type III elements, plate A and plate B has identical thickness and length. Therefore, the energy dissipated E_{III} was expressed according to Eq. (6) as

$$E_{\mathrm{III}} = 1/4\sigma_{\mathrm{o}}h_{\mathrm{A}}^2\left[8\frac{H^2}{h_{\mathrm{A}}}\left(\frac{\pi}{2} - \psi_{\mathrm{IIIo}}\right) + 4\pi C_{\mathrm{A}} + 2H(\pi - 2\psi_{\mathrm{IIIo}})\right] \tag{10}$$

Again, the expression of E_{IV} was similar to E_{III} and hence not presented.

Energy balance dictated that the mean crushing force could be expressed as [8]

$$P_{\mathrm{m}} = 5(2E_{\mathrm{I}} + 2E_{\mathrm{II}} + E_{\mathrm{III}} + E_{\mathrm{IV}})/(H\xi) \tag{11}$$

The identified parameters were: length of cross section C, wall thickness h, angle ψ_{o} of a given element, effective crush distance coefficient ξ, and flow stress σ_{o}. The value of ξ was 0.73 according to Ref. [8] and the flow stress was calculated from the energy

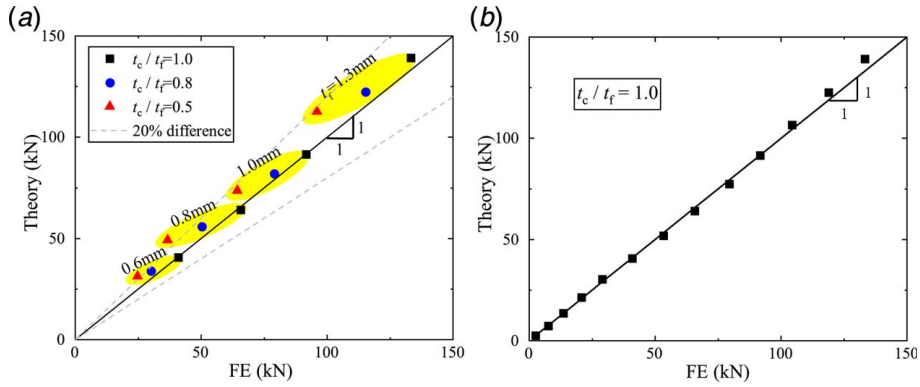

Fig. 13 Correlation of the theoretically predicted and numerically calculated mean crushing forces for sandwich structures with (*a*) different thickness ratios t_c/t_f and (*b*) fixed thickness ratio ($t_c/t_f = 1$)

equivalent stress, as [32]

$$\sigma_o = \sqrt{\frac{\sigma_u \sigma_y}{1+n}} \tag{12}$$

However, the half-length of the fold H and the radius of toroidal surface b were unknown and needed to be solved. Thus, the crushing force was a function of H and b. Since the actual crushing process leads to the minimum mean crushing force [6], one has

$$\frac{\partial P_m}{\partial H} = 0, \quad \frac{\partial P_m}{\partial b} = 0 \tag{13}$$

Substituting Eq. (11) into Eq. (13), H and b could be determined, and thus the mean crushing force P_m was obtained. The resulting explicit expression of P_m was too onerous to be written, so only numerical solutions of P_m were obtained with MATLAB. In MATLAB, the energy dissipated in the basic folding elements E_I–E_{IV} was calculated separately according to Eqs. (7)–(10) in the first place, where the unknown parameter H and b were included in the expressions. After summing up the dissipated energy in all folding elements, the expressions of P_m with respect to H and b were got according to Eq. (11). Afterward, the "fsolve" function was used to solve H and b in Eq. (13) and finally P_m was calculated based on the known H and b.

It should be noticed that, when applying the method of "super folding elements," the thickness of the two plates in one element was identical, represented by h. However, for type I–II elements in the current study, the facesheets (Plate A) and the corrugated plates (Plate B) might have different thicknesses. Thus, with equal thickness assumed for both the facesheets and corrugated plates, h was replaced by the average thickness of Plate A and Plate B, i.e., $(h_A + h_B)/2$. The effectiveness of this equivalence and the likely difference arising from it were evaluated in Sec. 6.

6 Discussions

6.1 Comparison Between Finite Element Simulation Results and Theoretical Predictions. To validate the present theoretical model, correlation of the calculated mean crushing force between model predictions and FE simulations was illustrated in Fig. 13. The numerically simulated crushing force was taken as the abscissa, while the theoretically predicted one was taken as the ordinate. The correlation could be reflected by deviation of the coordinates from the line with a slope of 1. For example, excellent agreement could be obtained when the point fell onto this line, while the difference between numerical and theoretical results would increase as the coordinate deviated from the black line. As a reference, 20% difference lines were also plotted in Fig. 13.

In Fig. 13(*a*), the coordinates for cases when the facesheet thickness t_f lied in the range of 0.6 mm–1.3 mm resided in the yellow elliptic regions. Specifically, t_c/t_f was selected as 0.5, 0.8, and 1.0 for each t_f. It was seen from Fig. 13(*a*) that the correlation between the theoretical and simulated results was satisfactory. For the cases of $t_c/t_f = 1$, the calculation points exactly fell onto the line with a slope of 1, demonstrating excellent correlation. As t_c/t_f was decreased to 0.8, the deviation increased, but all the points still stayed within the 20% difference region. When t_c/t_f was fixed at 0.5, the deviation increased further and some coordinates fell out of the 20% difference region. The increased deviation was induced by increased inconsistency in the thickness of facesheets and corrugated plates, which reduced the accuracy of theoretical model predictions. Recall that, when calculating M_o in type I–II elements, h in Eq. (3) was hypothetically replaced by $(h_A + h_B)/2$, namely, $(t_c + t_f)/2$. In other words, the results of Fig. 13(*a*) suggested that inconsistency in the thickness of facesheets and corrugated plates led to difference of theoretical predictions.

As for the specific case of $t_c/t_f = 1$, Fig. 13(*b*) presented the simulated and theoretical results for t_f varying from 0.1 mm to 1.3 mm. Excellent correlation was found for all the coordinates. Thus, the theoretical model was effective for predicting the mean crushing force of the CSCSs when its facesheets and corrugated members have approximately the same thickness.

6.2 Parametric Study. Next, a parametric study was carried out using the theoretical model developed to quantify the effects of N, W/R_o, and t_c/t_f on mean crushing force, as shown in Fig. 14. It should be noticed that for all the cases examined, the weight of the CSCS structure remained constant. The effect of N on P_m for cases of different t_c/t_f but fixed W/R_o ($W/R_o = 0.21$) was presented in Fig. 14(*a*). As N was increased, P_m increased but the rate of increase slowed down. Given a specific N, the CSCS with a larger t_c/t_f exhibited a larger P_m. Figure 14(*b*) presented the effect of N on P_m for cases of different W/R_o but fixed t_c/t_f ($t_c/t_f = 1.0$). Similar to Fig. 14(*a*), P_m increased and the rate of increase slowed down when N was increased. Nevertheless, the influence of W/R_o on P_m was a little complicated. For cases with N less than 12, P_m increased with increasing W/R_o; while for cases with N exceeding 17, a larger W/R_o usually led to a higher P_m. As reference, the P_m of a monolithic cylindrical shell (i.e., the single-cell shell) with equal mass, calculated using the formula detailed in Ref. [57], was also added to Fig. 14. All the present CSCS structures showed much better energy absorption capacities than the monolithic cylindrical shell.

6.3 Dynamic Impact. Generally, compared with quasi-static compression, the mean crushing force of a thin-walled tubular structure would increase when subjected to dynamic impact. For CSCS structures considered in the current study, since their parent materials (aluminum alloys) are insensitive to strain rate, the effect of

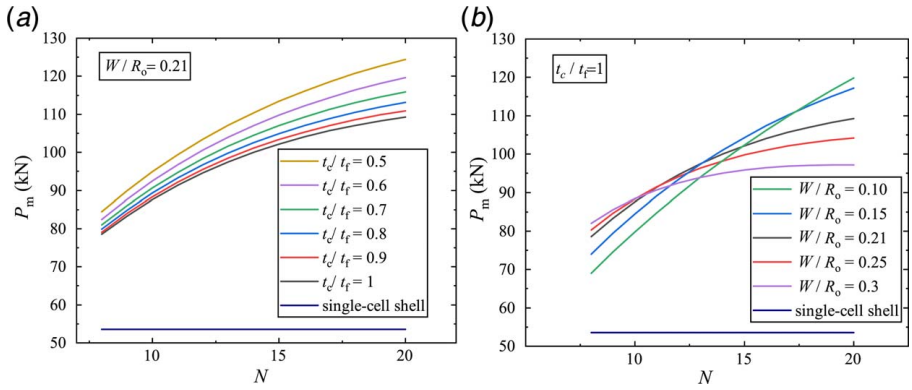

Fig. 14 Mean crushing force versus the number of corrugated units along the circumference of CSCS structure for (*a*) fixed W/R_o with varying t_c/t_f and (*b*) fixed t_c/t_f with varying W/R_o. Single-cell shell denoted the monolithic cylindrical shell with equal mass.

dynamic crushing mainly results from inertia forces arising from the acceleration of shell walls [30]. The dynamic amplification coefficient D_{amp} was thence introduced to describe the dynamic effects, defined as

$$P_{m,d} = D_{amp} P_m \tag{14}$$

For a single-cell square tube, Hanssen et al. [30] presented the following expression of D_{amp}:

$$D_{amp} = 1 + C_{ine}\left(\frac{C-h}{h}\frac{\rho_o}{\sigma_o}v_o^2\right)^{1/2} \tag{15}$$

where C, h, and v_o denoted separately the cross section width of the square tube, the wall thickness, the impact velocity, and C_{ine} is a constant. It was seen from Eq. (15) that D_{amp} was proportional to v_o and inversely proportional to h.

By using FE simulation results and empirical theoretical predictions based on single-cell square tubes (i.e., Eq. (15)), the effect of impact velocity and wall thickness on D_{amp} was qualitatively illustrated in Fig. 15. The FE model was the same as that described in Sec. 4. The material properties used in the dynamic simulations were also the same as those used in the static case, since the aluminum alloy was not sensitive to the strain rate [30]. Differently, the pressure plate was given a mass of 600 kg and had an initial velocity. In the theoretical analysis, C in Eq. (15) was the average length of folding elements displayed in Fig. 12, and the constant C_{ine} was obtained to have a value of 0.3 by fitting the simulated results.

Figure 15(*a*) presented the force versus displacement curves of a CSCS with $t_f = t_c = 0.8$ mm for selected impact velocities. Due to inertia effects, the curve of high impact velocity was higher than that of low velocity, i.e., the mean crushing force somewhat increased as the impact velocity was increased. The D_{amp} calculated from FE simulations for CSCSs having different wall thicknesses (assuming $t_f = t_c$) was presented in Fig. 15(*b*). It was seen that D_{amp} decreased with the increase of the wall thickness. For a specific wall thickness, a higher impact velocity led to a higher D_{amp}. Theoretical predictions of D_{amp} were also plotted with dash lines in Fig. 15(*b*). Although there were some fluctuations for the D_{amp} versus thickness curves obtained from FE simulations, the trend of the curve obtained from simulations was qualitatively coincident with that predicted via theoretical analysis. The quantitative difference was mainly attributed to the much more complex cross-sectional shape of the present CSCS structure, compared with single-cell square tubes.

7 Conclusions

The energy adsorption performance of CSCSs was systematically investigated using the method combining experiments, simulations, and theoretical analysis. Main conclusions were summarized as follows:

(1) CSCS specimens fabricated via either the high-speed wire-cut electric discharge machining (HSWEDM) or extrusion approach both exhibited stable crushing behavior under quasi-static axial compression, even at large deformations. Axisymmetric collapse occurred and the final folding deformation was consisted of periodic sub-folds along the circumference (ten such folds in total for the present specimens) as well as periodic sub-folds in the axial direction (five such folds in total, but could have more if the CSCS specimens had a

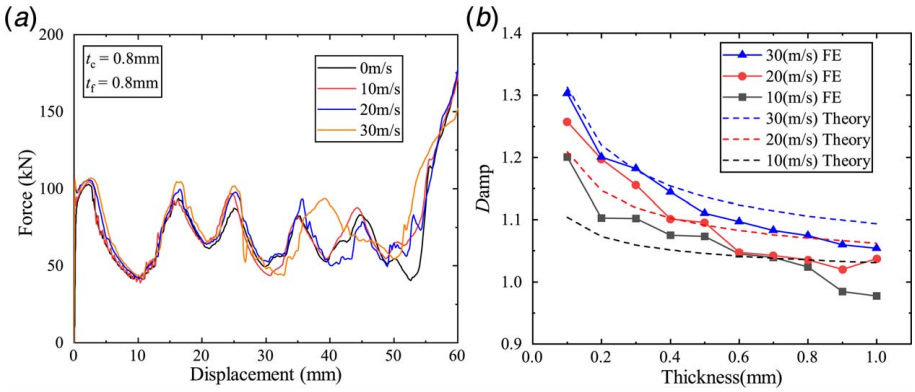

Fig. 15 Effect of dynamic impact on (*a*) displacement versus force curves and (*b*) D_{amp} versus wall thickness curves for CSCSs with $t_f = t_c$

larger height), named here as the "localized axisymmetric folding mode". Benefited from the stable folding deformation mode, the CSCSs possess good energy absorption capacity and high reliability in actual application of impact resistance.

(2) CSCS specimens fabricated via HSWEDM experienced local ruptures under axial compression, while those fabricated via extrusion showed good ductility and no rupture occurred throughout the compression. Besides, the fabrication cost of the extrusion specimens was much less than the HSWEDM ones. Excellent energy absorption, high repeatability and low cost make the extruded CSCSs ideal energy absorption structures.

(3) For all the CSCS specimens, the simulated force versus displacement curves as well as the corresponding folding deformation mode compared well with those obtained experimentally. With the method of super folding elements, a theoretical model was constructed on the basis of this new type of folding mode to calculate approximately the mean crushing force of the CSCS structure. Excellent correlation between numerically simulated and theoretically predicted results was obtained, particularly when the facesheets and corrugated members had roughly the same thickness.

(4) Under dynamic impact, the dynamic amplification coefficient D_{amp} of the CSCS structures decreased with the increase of wall thickness (assuming the facesheets and corrugated members had identical thickness) and increased as the impact velocity was increased.

Acknowledgment

This work was supported by the National Natural Science Foundation of China (11802221, 51875441, and 11972185), the National Key R&D Program of China (2018YFB1106400), the Zhejiang Provincial Natural Science Foundation of China (LGG18A020001), and the Open Fund of the State Key Laboratory of Mechanics and Control of Mechanical Structures (Nanjing University of Aeronautics and astronautics, MCMS-I-0219K01 and MCMS-E0219K02).

Conflict of Interest

There are no conflicts of interest.

Data Availability Statement

The datasets generated and supporting the findings of this article are obtainable from the corresponding author upon reasonable request. The authors attest that all data for this study are included in the paper.

Nomenclature

- b = radius of toroidal surface in the super folding elements
- d = actual crushed deformation
- h = shell thickness of super folding elements
- n = power-law coefficient
- C = length of the super folding elements
- E = total energy absorbed
- H = half-length of the fold
- N = number of corrugated units
- W = core width
- t_c = core thickness
- t_f = facesheets thickness
- v_o = impact velocity
- A_E = crush force efficiency
- C_{ine} = dynamic amplification constant
- D_{amp} = dynamic amplification coefficient
- F_m = mean crushing force
- F_{max} = maximum force
- H_s = original height of cylindrical shell
- R_i = radius of inner facesheet
- R_o = radius of outer facesheet
- S_E = stroke efficiency
- T_E = total efficiency
- ϵ_u = strain corresponding to ultimate stress σ_u
- ξ = effective crush distance coefficient
- $\sigma_{0.2}$ = stress at 0.2% plastic strain
- σ_o = flow stress
- σ_u = ultimate stress
- Φ = circumferential coordinates of the toroidal surface
- ψ_o = angle of super folding elements

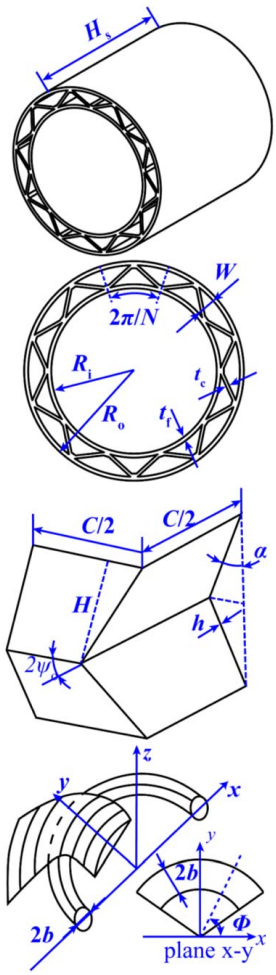

Table 2 Comparisons among different fabrication methods[a]

Specimens	$\sigma_{0.2}$ (MPa)	F_{max} (kN)	F_m (kN)	A_E	SEA (J/kg)	Unit price ($)	Wall thickness (mm)
Adhesive #1	140.00	19.60	5.90	0.30	7.33		<0.5
Adhesive #2	140.00	48.30	15.50	0.32	10.44		
HSWEDM	229.00	160.91	100.60	0.63	41.14	200	>1
Extrusion	175.00	136.62	101.52	0.74	36.12	1.5	

[a]Adhesive samples were prepared only under laboratory conditions involving tedious manual procedures and hence it was difficult to evaluate the unit price.

Appendix: Comparisons Among Different Fabrication Methods

Table 2 compared CSCS specimens fabricated using the two different methods in the current study work and the preparation method adopted in our previous study [51]. The unit price in Table 2 referred to the production cost of one specimen when the production quantity exceeded 1000. Adhesive #1/#2 represented specimens fabricated in Ref. [51].

It was seen that specimens fabricated in this work showed better crush force efficiency (A_E) and specific energy absorption (SEA) compared with those fabricated in the previous work. Besides, the method used in the previous work was proposed based on laboratory conditions and hence not viable for mass production. However, both the HSWEDM and extrusion processes adopted in the present study are mature industrial preparation methods. It was therefore not surprising that the present specimens exhibited better energy absorption capacity and practicability in comparison with those reported in Ref. [51]. It could also be seen from Table 2 that the SEA of HSWEDM specimens was 14% higher than that of extrusion specimens, while the unit price of extrusion specimens was only 1% of that of HSWEDM specimens.

References

[1] Lu, G., and Yu, T., 2003, *Energy Absorption of Structures and Materials*, Woodhead Publishing Ltd., Cambridge.
[2] Zhang, Z., Liu, S., and Tang, Z., 2011, "Comparisons of Honeycomb Sandwich and Foam-Filled Cylindrical Columns Under Axial Crushing Loads," Thin Walled Struct., **49**(9), pp. 1071–1079.
[3] Alexander, J. M., 1960, "An Approximate Analysis of the Collapse of Thin Cylindrical Shells Under Axial Loading," Q. J. Mech. Appl. Math., **13**(1), pp. 10–15.
[4] Abramowicz, W., and Jones, N., 1984, "Dynamic Axial Crushing of Circular Tubes," Int. J. Impact Eng., **2**(3), pp. 263–281.
[5] Abramowicz, W., and Jones, N., 1986, "Dynamic Progressive Buckling of Circular and Square Tubes," Int. J. Impact Eng., **4**(4), pp. 243–270.
[6] Wierzbicki, T., and Abramowicz, W., 1983, "On the Crushing Mechanics of Thin-Walled Structures," ASME J. Appl. Mech., **50**(4a), pp. 727–734.
[7] Abramowicz, W., and Jones, N., 1984, "Dynamic Axial Crushing of Square Tubes," Int. J. Impact Eng., **2**(2), pp. 179–208.
[8] Abramowicz, W., and Wierzbicki, T., 1989, "Axial Crushing of Multicorner Sheet Metal Columns," ASME J. Appl. Mech., **56**(1), pp. 113–120.
[9] Mamalis, A. G., Manolakos, D. E., Ioannidis, M. B., Kostazos, P. K., and Dimitriou, C., 2003, "Finite Element Simulation of the Axial Collapse of Metallic Thin-Walled Tubes With Octagonal Cross-Section," Thin Walled Struct., **41**(10), pp. 891–900.
[10] Zhang, X., and Zhang, H., 2012, "Experimental and Numerical Investigation on Crush Resistance of Polygonal Columns and Angle Elements," Thin Walled Struct., **57**, pp. 25–36.
[11] Xiang, Y., Yu, T., and Yang, L., 2016, "Comparative Analysis of Energy Absorption Capacity of Polygonal Tubes, Multi-Cell Tubes and Honeycombs by Utilizing Key Performance Indicators," Mater. Des., **89**, pp. 689–696.
[12] Tabacu, S., and Ducu, C., 2019, "An Analytical Solution for the Estimate of the Mean Crushing Force of Structures With Polygonal and Star-Shaped Cross-Sections Subjected to Axial Load," Int. J. Mech. Sci., **161**.
[13] Fan, Z., Lu, G., Yu, T. X., and Liu, K., 2013, "Axial Crushing of Triangular Tubes," Int. J. Appl. Mech., **5**(1), p. 13500008.
[14] Deng, X., Liu, W., and Lin, Z., 2018, "Experimental and Theoretical Study on Crashworthiness of Star-Shaped Tubes Under Axial Compression," Thin Walled Struct., **130**, pp. 321–331.
[15] Deng, X., Liu, W., and Jin, L., 2018, "On the Crashworthiness Analysis and Design of a Lateral Corrugated Tube With a Sinusoidal Cross-Section," Int. J. Mech. Sci., **141**, pp. 330–340.
[16] Tang, Z., Liu, S., and Zhang, Z., 2012, "Energy Absorption Properties of Non-Convex Multi-Corner Thin-Walled Columns," Thin Walled Struct., **51**, pp. 112–120.
[17] Tang, Z., Liu, S., and Zhang, Z., 2013, "Analysis of Energy Absorption Characteristics of Cylindrical Multi-Cell Columns," Thin Walled Struct., **62**, pp. 75–84.
[18] Chen, W., and Wierzbicki, T., 2001, "Relative Merits of Single-Cell, Multi-Cell and Foam-Filled Thin-Walled Structures in Energy Absorption," Thin Walled Struct., **39**(4), pp. 287–306.
[19] Zhang, X., Cheng, G., and Zhang, H., 2006, "Theoretical Prediction and Numerical Simulation of Multi-Cell Square Thin-Walled Structures," Thin Walled Struct., **44**(11), pp. 1185–1191.
[20] Zhang, X., and Zhang, H., 2012, "Numerical and Theoretical Studies on Energy Absorption of Three-Panel Angle Elements," Int. J. Impact Eng., **46**, pp. 23–40.
[21] Zhang, X., and Zhang, H., 2013, "Energy Absorption Limit of Plates in Thin-Walled Structures Under Compression," Int. J. Impact Eng., **57**, pp. 81–98.
[22] Zhang, X., and Zhang, H., 2013, "Theoretical and Numerical Investigation on the Crush Resistance of Rhombic and Kagome Honeycombs," Compos. Struct., **96**, pp. 143–152.
[23] Ding, X., Tong, Z., Liu, Y., and Liu, S., 2018, "Dynamic Axial Crush Analysis and Design Optimization of a Square Multi-Cell Thin-Walled Tube With Lateral Variable Thickness," Int. J. Mech. Sci., **140**, pp. 13–26.
[24] Liu, S., Tong, Z., Tang, Z., Liu, Y., and Zhang, Z., 2015, "Bionic Design Modification of Non-Convex Multi-Corner Thin-Walled Columns for Improving Energy Absorption Through Adding Bulkheads," Thin Walled Struct., **88**, pp. 70–81.
[25] Fan, H., Luo, Y., Yang, F., and Li, W., 2018, "Approaching Perfect Energy Absorption Through Structural Hierarchy," Int. J. Eng. Sci., **130**, pp. 12–32.
[26] Reid, S. R., 1993, "Plastic Deformation Mechanisms in Axially Compressed Metal Tubes Used as Impact Energy Absorbers," Int. J. Mech. Sci., **35**(12), pp. 1035–1052.
[27] Reddy, T. Y., and Wall, R. J., 1988, "Axial Compression of Foam-Filled Thin-Walled Circular Tubes," Int. J. Impact Eng., **7**(2), pp. 151–166.
[28] Kavi, H., Toksoy, A. K., and Guden, M., 2006, "Predicting Energy Absorption in a Foam-Filled Thin-Walled Aluminum Tube Based on Experimentally Determined Strengthening Coefficient," Mater. Des., **27**(4), pp. 263–269.
[29] Hanssen, A. G., Langseth, M., and Hopperstad, O. S., 2000, "Static and Dynamic Crushing of Circular Aluminium Extrusions With Aluminium Foam Filler," Int. J. Impact Eng., **24**(5), pp. 475–507.
[30] Hanssen, A. G., Langseth, M., and Hopperstad, O. S., 2000, "Static and Dynamic Crushing of Square Aluminium Extrusions With Aluminium Foam Filler," Int. J. Impact Eng., **24**(4), pp. 347–383.
[31] Santosa, S., and Wierzbicki, T., 1998, "Crash Behavior of Box Columns Filled With Aluminum Honeycomb or Foam," Comput. Struct., **68**(4), pp. 343–367.
[32] Santosa, S. P., Wierzbicki, T., Hanssen, A. G., and Langseth, M., 2000, "Experimental and Numerical Studies of Foam-Filled Sections," Int. J. Impact Eng., **24**(5), pp. 509–534.
[33] Zarei, H., and Kröger, M., 2008, "Optimum Honeycomb Filled Crash Absorber Design," Mater. Des., **29**(1), pp. 193–204.
[34] Sun, G., Li, G., Hou, S., Zhou, S., Li, W., and Li, Q., 2010, "Crashworthiness Design for Functionally Graded Foam-Filled Thin-Walled Structures," Mater. Sci. Eng. A, **527**(7), pp. 1911–1919.
[35] Yin, H., Wen, G., Fang, H., Qing, Q., Kong, X., Xiao, J., and Liu, Z., 2014, "Multiobjective Crashworthiness Optimization Design of Functionally Graded Foam-Filled Tapered Tube Based on Dynamic Ensemble Metamodel," Mater. Des., **55**, pp. 747–757.
[36] Zhu, G., Li, S., Sun, G., Li, G., and Li, Q., 2016, "On Design of Graded Honeycomb Filler and Tubal Wall Thickness for Multiple Load Cases," Thin Walled Struct., **109**, pp. 377–389.
[37] Cui, L., Kiernan, S., and Gilchrist, M. D., 2009, "Designing the Energy Absorption Capacity of Functionally Graded Foam Materials," Mater. Sci. Eng. A, **507**(1–2), pp. 215–225.
[38] Zhang, Z., Liu, S., and Tang, Z., 2010, "Crashworthiness Investigation of Kagome Honeycomb Sandwich Cylindrical Column Under Axial Crushing Loads," Thin Walled Struct., **48**(1), pp. 9–18.
[39] Xue, Z., and Hutchinson, J. W., 2004, "A Comparative Study of Impulse-Resistant Metal Sandwich Plates," Int. J. Impact Eng., **30**(10), pp. 1283–1305.
[40] Han, B., Zhang, Z., Zhang, Q., Zhang, Q., Lu, T. J., and Lu, B., 2017, "Recent Advances in Hybrid Lattice-Cored Sandwiches for Enhanced Multifunctional Performance," Extreme Mech. Lett., **10**, pp. 58–69.
[41] Han, B., Qin, K., Yu, B., Wang, B., Zhang, Q., and Lu, T. J., 2016, "Honeycomb–Corrugation Hybrid as a Novel Sandwich Core for Significantly Enhanced Compressive Performance," Mater. Des., **93**, pp. 271–282.
[42] Bin, H., Bo, Y., Yu, X., Chang-Qing, C., Qian-Cheng, Z., and Jian, L. T., 2015, "Foam Filling Radically Enhances Transverse Shear Response of Corrugated Sandwich Plates," Mater. Des., **77**, pp. 132–141.
[43] Xu, A., Vodenitcharova, T., Kabir, K., Flores-Johnson, E. A., and Hoffman, M., 2014, "Finite Element Analysis of Indentation of Aluminium Foam and Sandwich Panels With Aluminium Foam Core," Mater. Sci. Eng. A, **599**, pp. 125–133.
[44] Pollien, A., Conde, Y., Pambaguian, L., and Mortensen, A., 2005, "Graded Open-Cell Aluminium Foam Core Sandwich Beams," Mater. Sci. Eng. A, **404**(1), pp. 9–18.

[45] Mohan, K., Yip, T. H., Idapalapati, S., and Chen, Z., 2011, "Impact Response of Aluminum Foam Core Sandwich Structures," Mater. Sci. Eng. A, **529**, pp. 94–101.
[46] Yan, L. L., Yu, B., Han, B., Zhang, Q. C., Lu, T. J., and Lu, B. H., 2020, "Effects of Aluminum Foam Filling on the Low-Velocity Impact Response of Sandwich Panels With Corrugated Cores," J. Sandwich Struct. Mater., **22**(4), pp. 929–947.
[47] Zheng, G., Wu, S., Sun, G., Li, G., and Li, Q., 2014, "Crushing Analysis of Foam-Filled Single and Bitubal Polygonal Thin-Walled Tubes," Int. J. Mech. Sci., **87**, pp. 226–240.
[48] Liu, W., Lin, Z., He, J., Wang, N., and Deng, X., 2016, "Crushing Behavior and Multi-Objective Optimization on the Crashworthiness of Sandwich Structure With Star-Shaped Tube in the Center," Thin Walled Struct., **108**, pp. 205–214.
[49] Li, W., Sun, F., Wei, W., Liu, D., Zhang, X., Li, M., and Fan, H., 2018, "Fabrication and Testing of Composite Corrugated-Core Sandwich Cylinder," Compos. Sci. Technol., **156**, pp. 127–135.
[50] Jiang, S., Sun, F., and Fan, H., 2017, "Multi-Failure Theory of Composite Orthogrid Sandwich Cylinder," Aerosp. Sci. Technol., **70**, pp. 520–525.
[51] Xiong, J., Feng, L., Ghosh, R., Wu, H., Wu, L., Ma, L., and Vaziri, A., 2016, "Fabrication and Mechanical Behavior of Carbon Fiber Composite Sandwich Cylindrical Shells With Corrugated Cores," Compos. Struct., **156**, pp. 307–319.
[52] Yang, J., Xiong, J., Ma, L., Feng, L.-N., Wang, S., and Wu, L., 2015, "Modal Response of All-Composite Corrugated Sandwich Cylindrical Shells," Compos. Sci. Technol., **115**, pp. 9–20.
[53] Han, Y., Wang, P., Fan, H., Sun, F., Chen, L., and Fang, D., 2015, "Free Vibration of CFRC Lattice-Core Sandwich Cylinder With Attached Mass," Compos. Sci. Technol., **118**, pp. 226–235.
[54] Yang, M., Han, B., Su, P., Wei, Z., Zhang, Q., Zhang, Q., and Lu, T. J., 2020, "Free Vibration and Axial Compression of All-Metallic Cylindrical and Truncated Conical Sandwich Shells With Corrugated Cores," J. Sandwich Struct. Mater.
[55] Su, P.-B., Han, B., Yang, M., Wei, Z.-H., Zhao, Z.-Y., Zhang, Q.-C., Zhang, Q., Qin, K.-K., and Lu, T. J., 2018, "Axial Compressive Collapse of Ultralight Corrugated Sandwich Cylindrical Shells," Mater. Des., **160**, pp. 325–337.
[56] Zhang, X., and Zhang, H., 2014, "Axial Crushing of Circular Multi-Cell Columns," Int. J. Impact Eng., **65**, pp. 110–125.
[57] Guillow, S. R., Lu, G., and Grzebieta, R. H., 2001, "Quasi-Static Axial Compression of Thin-Walled Circular Aluminium Tubes," Int. J. Mech. Sci., **43**(9), pp. 2103–2123.